PROCEEDINGS, 45th Workshop on Geothermal Reservoir Engineering
Stanford University, Stanford, California, February 10-12, 2020
SGP-TR-216

Looking at Fracture Sealing Mechanisms by Granular LCM at Elevated Temperatures

Lu Lee and Arash Dahi Taleghani

Penn State University, University Park, PA 16802
Email: arash.dahi@psu.edu

Keywords: lost circulation; CFD-DEM; drilling fluid; fracture sealing; geothermal

ABSTRACT

Lost circulation occurs when the returned fluid is less than what is pumped into the well due to loss of fluid to pores or fractures. A lost-circulation event is a common occurrence in a geothermal well. Typical geothermal reservoirs are often underpressured and have larger fracture apertures. A severe lost-circulation event is costly and can lead to stuck pipe, well instability, and well abandonment. One typical treatment is adding lost-circulation materials (LCMs) to seal fractures. Conventional LCMs fail to properly seal fractures because their mechanical limit is exceeded at elevated temperatures. In this paper, parametric studies in numerical simulation are conducted to better understand different thermal effects on the sealing mechanisms of LCMs. The computational fluid dynamics (CFD) and discrete element method (DEM) are coupled as to accurately capture the true physics of sealing by granular materials. Due to computational limits, traditional Eulerian-Eulerian approach treats solid particles as a group of continuum matter. With the advance of modern computational power, particle bridging is achievable with DEM to track individual particles by modeling their interactive forces between each other. Particle-fluid interactions can be modeled by coupling CFD algorithms. Fracture sealing capability is investigated by studying the effect of four individual properties including fluid viscosity, particle size, friction coefficient, and Young's modulus. It is found that thermally degraded properties lead to inefficient fracture sealing.

1. INTRODUCTION

Geothermal energy by its name is a heat source existing underground, which can be extracted or exploited. A successful drilling and completion operation of a geothermal well is important because the extraction of geothermal energy relies on circulating high temperature fluids from a target depth for heat exchange. Geothermal reservoirs exhibit temperatures ranging from 160 to above 300 °C (320 to 572 °F), high compressive strength of 240+ MPa, and highly fractured formations (Finger and Blankenship, 2010). The primary challenge of drilling a geothermal well is that its reservoir is typically under-pressured, and its natural fractures show large apertures on the order of centimeters. Therefore, lost circulation is usually anticipated and should be prevented or remediated. Lost circulation in drilling is defined as the total or partial loss of drilling fluids into highly permeable zones, cavernous formations, and natural or induced fractures. To cure lost circulation problems, LCMs can be added to drilling fluid to seal or bridge the fracture flow pathways. Failing to properly seal fractures and cure lost circulation could lead to stuck pipe, well instability, and loss of well. Fluid design for drilling ultrahigh temperature zones or geothermal wells should be considered by using a high thermal-resistant formula. Many specifications given in laboratory tested products are conducted in ambient temperature or within a thermal tolerance condition. According to Carson and Lin (1982), lost circulation and its associated problems represent at least an average of 15% increase in well cost at the most mature US geothermal area. Moreover, recent studies in Cole et al. (2017) also show that an estimated $185,000 or more is added to the cost (which averaged over 100 hours of unprogrammed nonproductive time) because of lost circulation events.

A typical drilling fluid formula contains some sort of LCM in anticipation of a lost-circulation situation. The fracture-sealing effectiveness depends on the size and mechanical strength of the LCM. Most of the LCMs available in the market can be categorized as either fibrous, flaky, or granular. In the recent years, developments have gone towards smart LCMs that are designed to expand in a targeted temperature range (Mansour et al., 2017; Mansour and Dahi Taleghani, 2018). Fibrous and flaky materials are out of the scope of this paper, and only granular materials are discussed. A mixture of rigid granular particles generally provides the best fracture-sealing capabilities (Messenger, 1981). However, fracture apertures in excess of 5 mm represent a serious challenge for currently available LCMs (Lavrov, 2016). If the size of the LCM is too large, it can also plug up downhole drilling equipment. Even though conventional LCMs work in a typical oil and gas sedimentary formation, it may not work at an elevated-temperature condition.

Mechanical properties of LCMs can be altered due to thermal effects such as particle degradation. When LCMs undergo the transport process, abrasion typically occurs but can be intensified by the increase of the downhole temperature. According to tests conducted by Loeppke (1990), the sealing capability is not improved by increasing concentrations of thermally degraded materials. This means that having larger quantities of the already degraded LCMs would not help or reduce the impact of a lost-circulation event. Additionally, rheological properties of the drilling fluid can be affected at elevated temperatures and consequently influence particle-particle and particle-fluid interactions. In this paper, thorough parametric studies are conducted to investigate how the sealing mechanisms of granular LCMs can be affected by the consequences of elevated temperatures.

2. DRILLING FLUIDS AT ELEVATED TEMPERATURES

2.1 Fluid Viscosity

The gel and rheological properties are strongly dependent on temperature. Liquid viscosity usually decreases with increasing temperature. However, water-based drilling fluids consists of mostly bentonite and clay constituents. They can flocculate in a high temperature environment. One way to control and decrease the flocculation temperature is to add lignosulfonate or other types of deflocculants. Deflocculants can also be thermally degraded, nulling the original intention of keeping rheological properties of the drilling fluid constant. Nevertheless, the fluid viscosity may increase or decrease depending on many factors including both physical behaviors and chemical reactions. Even though researchers have been developing better thermally resistant drilling fluids, it is still unavoidable for fluid viscosities to change due to temperature fluctuation such as the fluid samples seen in **Table 1**.

Table 1: **Drilling fluid viscosities at various temperatures**

Fluid Type	T (°C / °F)	Apparent Viscosity (mPa·s)	Plastic Viscosity (mPa·s)	Reference
Fresh-Water Based	20-240 / 68-464	88-70	67-33	Wang et al. (2012)
Brine-Based	20-240 / 68-464	47-148	31-34	
Water-Based with Iron Oxide Nanoparticle	25-85 / 77-185	(7.7-15.7) to (2.3-10.5)	(28.1-45.6) to (9.9-33.6)	Mohammed (2017)
Geothermal Spring	15-150 / 59-302	(11.18-19.7) to (1.867-8.551)	(6.92-10.65) to (2.282-6.707)	Avci and Mert (2019)

2.2 Particle Properties

Particles exposed to high temperature conditions can be thermally degraded. **Table 2** shows the tests conducted by Loeppke et al. (1990) that present some of commonly used LCMs in drilling fluids. They measured softening temperatures by placing the particles under compression in the elastic region of the stress and strain curve and slowly increasing the particle temperature. At the softening temperature, the particle strain increases drastically and continues with further increase of temperature until failure occurs.

Table 2: Granular material properties and softening temperatures (Loeppke et al., 1990)

Material	Compressive Strength (MPa)	Young's Modulus (MPa)	Softening Temperature (°C / °F)
Thermoset Rubber	14.00	43.64	110-192 / 43-89
Coal	1.45	12.96	250-330 / 121-166
Expanded Aggregate	5.93	44.20	> 500 / > 260
Gilsonite	2.34	12.00	345-375 / 174-191
Mixed Nut Shells	56.74	196.50	380-480 / 193-249
Black Walnut Shells	68.05	141.34	360-500 / 182-260

When choosing the appropriate size of LCM, Goodman (1981) gives a general rule for maximum particle diameter to be one-half of the fracture width and 5% fluid volume to be the bridging size. However, the LCM sizes degrade over time when the transport process takes place from surface equipment to the downhole environment. This is due to the rapid movement that causes shear and collisions between particles. Other attributes such as chemical reactions and thermally induced stresses can promote particle degradation as well. Furthermore, increase in temperature typically leads to decrease of viscosity resulting in less friction or resistant force for particulate flows. Smaller particle sizes, which can be induced by higher temperature, can also further induce particle degradation (Arena et al., 1983; Lin and Wey, 2005; Kang et al., 2019). All in all, particle degradation is aggravated by increase in temperature both directly and indirectly.

3. METHODOLOGY

3.1 Problem Description

The aim of this paper is to understand fracture sealing mechanisms of LCMs at elevated temperatures. The findings may help engineers modify their fluid recipes for drilling into high temperature zones and geothermal wells. Thus, sensitivity studies based on numerical simulations are conducted to investigate the sealing effectiveness of various properties. The properties include both LCM particles and drilling fluid. Thermal influence on LCM particles includes change in elasticity and size degradation. Therefore, Young's modulus, and size variations are investigated. The most notable fluid property change due to thermal effect is viscosity. Change of viscosity alters particle-fluid interactions, which may lead to undesired bridging.

3.2 CFD-DEM Coupling

The motions of LCMs carried by drilling fluid is simulated in a coupled CFD-DEM environment. The fluid-granular system under CFD-DEM framework is such that the fluid flow is calculated by OpenFOAM for CFD, and the motion of particles are resolved by LIGGGHTS for DEM (Goniva et al., 2012; Kloss et al., 2012). The basis and theory of the CFD-DEM technique have been comprehensively reviewed in Zhu et al. (2007; 2008). The conventional Eulerian-Eulerian approach assumes particles as another fluid-like phase. Transport models that consider solid particles in an Eulerian system do not capture the proper sealing phenomenon because solid particles are treated as another continuum. To achieve an accurate sealing mechanism of LCMs, it is better to track each particle in a Lagrangian manner although the trade-off is the consumption of more computational power.

Introduced by Cundall and Strack (1979), equilibrium forces are calculated and movement on individual particles are traced in DEM as

$$m_p \frac{d^2 x_p}{dt^2} = \boldsymbol{F}_{pn} + \boldsymbol{F}_{pt} + \boldsymbol{F}_{pf} + \boldsymbol{F}_{pb} \tag{1}$$

$$I_p \frac{d\boldsymbol{\omega}_p}{dt} = \boldsymbol{r}_{pc} \times \boldsymbol{F}_{pt} + \boldsymbol{T}_{pr} \tag{2}$$

where $\mathbf{F}_{pn}$ is the normal contact force, $\mathbf{F}_{pt}$ is the tangential contact force, $\mathbf{F}_{pf}$ is the force exerted from surrounding fluid to the particles, and $\mathbf{F}_{pb}$ is the body force of the particles. For particle rotational motion, I_p is the inertial tensor, $\mathbf{r}_{pc}$ is particle radius, and $\mathbf{T}_{pr}$ is the additional torque used to model non-sphericity by means of a rolling friction model.

The governing equations of unresolved CFD-DEM are given as

$$\frac{\partial \alpha_f}{\partial t} + \nabla \cdot \left(\alpha_f \boldsymbol{u}_f\right) = 0 \tag{3}$$

$$\frac{\partial\left(\alpha_f \rho_f \boldsymbol{u}_f\right)}{\partial t} + \nabla \cdot \left(\alpha_f \rho_f \boldsymbol{u}_f \boldsymbol{u}_f\right) = -\alpha_f \nabla p - K_{pf}\left(\boldsymbol{u}_f - \boldsymbol{u}_p\right) + \nabla \cdot \left(\alpha_f \boldsymbol{\tau}_f\right) \tag{4}$$

where α_f is the volume fraction of fluid, ρ_f is fluid density, K_{pf} is the implicit momentum exchange term of particle-fluid interactions, $\mathbf{u}_f$ is fluid velocity, $\mathbf{u}_p$ is the average particle velocity in one specified grid cell, and $\boldsymbol{\tau}_f$ is the stress tensor of fluid.

$$K_{pf} = \frac{\sum_i \boldsymbol{F}_{pf}}{V_{cell}\left|\boldsymbol{u}_f - \boldsymbol{u}_p\right|} \tag{5}$$

where V_{cell} is the volume of one specified grid cell.

Only pressure gradient force, buoyancy force, viscous force, and drag force are considered in the model. Di Felice's descriptions on drag force are adopted (Di Felice, 1994).

$$\boldsymbol{F}_{pf} = \frac{1}{8} C_d \rho_f \pi d_p^2 \left(\boldsymbol{u}_f - \boldsymbol{u}_p\right)\left|\boldsymbol{u}_f - \boldsymbol{u}_p\right| \alpha_f^{-\chi} \tag{6}$$

$$C_d = \left(0.63 + \frac{4.8}{\sqrt{Re_p}}\right)^2 \tag{7}$$

$$Re_p = \frac{\alpha_f \rho_f d_p \left|\boldsymbol{u}_f - \bar{\boldsymbol{u}}_p\right|}{\mu} \tag{8}$$

$$\chi = 3.7 - 0.65 e^{-\frac{\left(1.5 - \log_{10} Re_p\right)^2}{2}} \tag{9}$$

where C_d is the drag coefficient, d_p is particle diameter, χ is the empirical constant, Re_p is the particle Reynolds number, and μ is the fluid dynamic viscosity.

3.3 Model Setup and Input Parameters

A sketch of the fracture geometry is shown in **Figure 1**. Its length and height are 200 mm by 50 mm while inlet and outlet width are 1 mm and 0.5 mm respectively. Many researchers have investigated the appropriate grid cell to particle size in a fluidized bed simulation, but results differ with different methods used (Peng, 2014). Each grid cell is set to be 2 mm by 2 mm in length and height to ensure the accuracy and convergence of coupled CFD-DEM results. Every fracture wall is assumed to be in a no-slip boundary condition, and both inlet and outlet are under constant pressure. Fracture inlet is at 875 KPa (127 psi) and outlet pressure is at 0 KPa. The liquid phase is assumed to be Newtonian and incompressible. Gravity takes effect in the direction of downward fracture height.

Only single particle diameter is specified for every simulation for the purpose of studying the sealing mechanisms of monodispersed particles. Properties of the drilling fluid and particles are listed in **Table 3**, where base case is indicated in bold and italic. Simulation duration is 1 second with every timestep being 1 micro-second for both CFD and DEM. The coupling step of CFD-DEM is 100 DEM timestep. The solver uses a Pressure-Implicit Split-Operator (PISO) algorithm that is embedded in the CFDEM Coupling package (Issa, 1986).

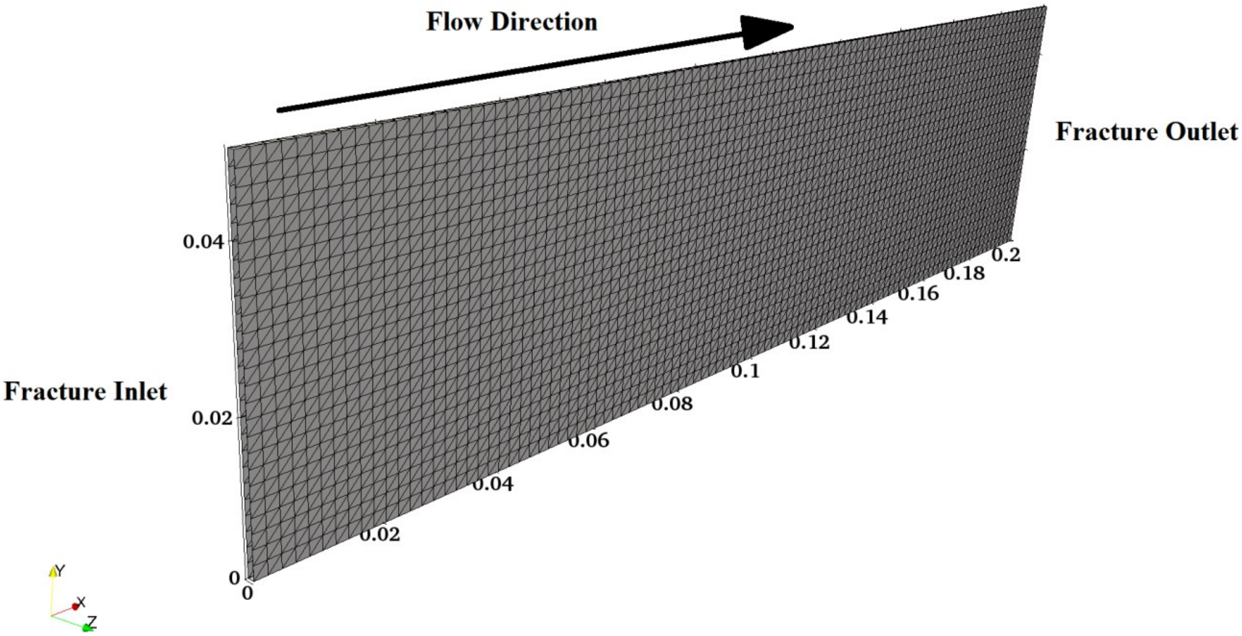

Figure 1: A sketch of the fracture geometry used in the numerical simulation (distance units in m).

Table 3: Properties of drilling fluid and particles (base/reference case in bold and italic).

Drilling Fluid	**Density (kg/m^3)**	2,000
	Viscosity (MPa·s)	0.3 / 3 / 30 / ***60*** / 90 / 120
Particles	**Diameter (mm)**	0.3 / 0.4 / ***0.5*** / 0.6 / 0.7 / 0.8 / 0.9
	Density (kg/m^3)	2500
	Young's Modulus (GPa)	0.1 / ***1*** / 10 / 50 / 100
	Poisson's Ratio	0.2 / ***0.3*** / 0.4 / 0.5
	Friction Coefficient	0 / 0.2 / 0.4 / ***0.6*** / 0.8 / 1
	Restitution Coefficient	0.5

4. RESULTS AND DISCUSSION

4.1 Fracture Sealing and Force Chain

In order to study the fracture sealing mechanism, interparticle forces are examined in each simulated case. For example, **Figure 2** shows a case of fracture bridging by LCMs along with its interactive force chains. This is commonly seen in other cases that have successful bridging as one can notice a network of force chains at the bridged location. A typical sealing process is shown in **Figure 3**, where a small amount of interparticle forces start building at a location inside the fracture. These force chains grow with more incoming particles, resulting in the bridging of fracture space. **Figure 3a** exhibits the beginning of decreasing flowrate at the fracture outlet due to initial particle bridging. In this stage, many particles are still able to flow through the soon-to-be bridged location. In **Figure 3b**, flowrate becomes constant when there is no more bridging taking place in the simulation. The fracture space has been filled up with LCMs starting from the initial bridging location all the way back to the fracture inlet. Broadly speaking, there are three stages during the sealing or bridging process. First, initial particle packing occurs in any given fracture location. This is seen around the peak of flowrate. Second, the faster trailing particles collide and interact with the slower frontal particles, which leads to larger particle packs. This is in the region of declining flowrate. Lastly, once the complete seal forms, the flowrate stabilizes at a lower flow. The difference between the peak flow and constant flow is how long it takes for a successful seal to form. Dimensionless volume is designed to indicate the severity of fluid loss for the duration of simulation time. It is the ratio of injected fluid volume to fracture volume.

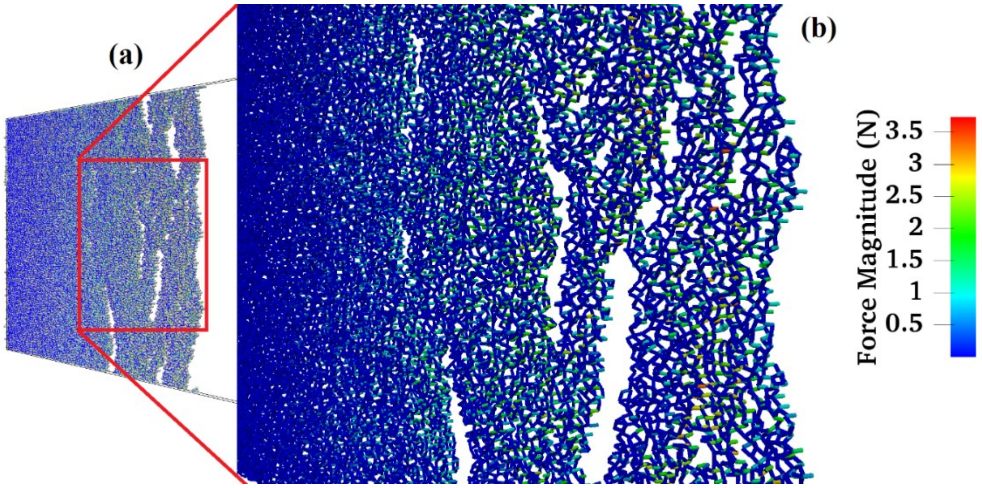

Figure 2: Fracture bridging. (a) LCM particles and force chains. (b) A closer view of force chain network near the fracture inlet.

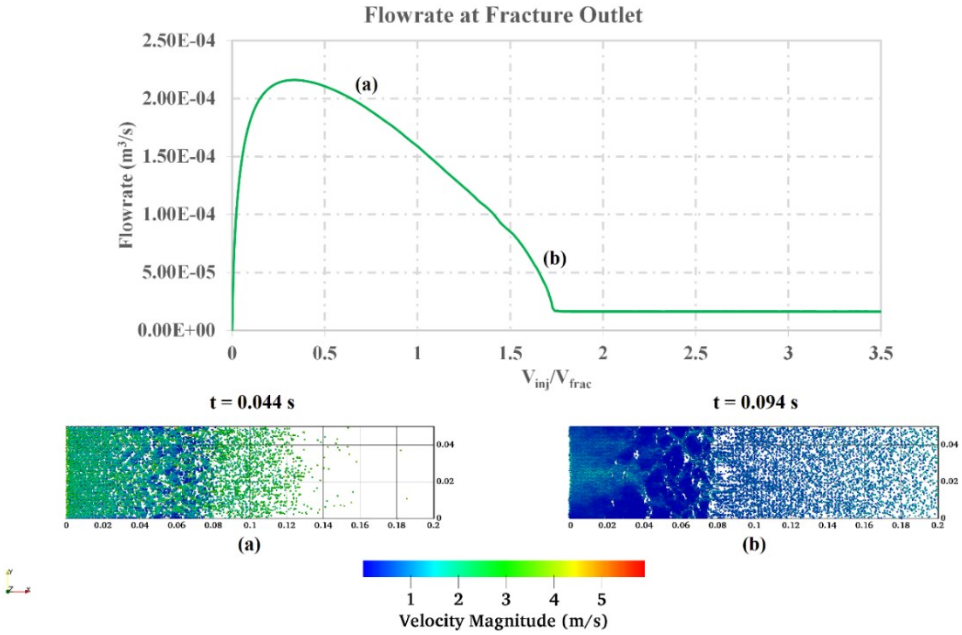

Figure 3: Particle buildup forming a bridge. (a) Initial buildup of few particles leading to a decline of flowrate. (b) Flowrate stabilized for a complete buildup of particles.

4.2 Fracture Sealing Capability of Thermally Affected Fluid Viscosity

Fluid viscosity can be easily altered at elevated temperatures. As shown in **Figure 4**, six different cases of fluid viscosities have been simulated and studied. Two of the lowest viscosity cases yielded unsuccessful sealing results, which can be seen by the large amount of flowrate at the fracture outlet as well as the large dimensionless volume in **Figure 4a**. On the other hand, the other four higher viscosity cases yielded successful sealing results in **Figure 4b**. Higher fluid viscosity leads to faster bridging as indicated by smaller dimensionless volume, although their final bridging locations are relatively similar to each other (around 70 mm more or less from the inlet), as shown in **Figure 6**.

It is worth noting that the lowest fluid viscosity (0.3 mPa·s) displays turbulent flow. This explains the spikes in **Figure 4a**. A snapshot of such a situation is shown in **Figure 5**, where packs of particles are distorted and have swept the surrounding area. This turbulent effect dissipates when the distorted particle movement reaches the fracture inlet. The highest particle velocity magnitude exhibits as high as 40+ m/s.

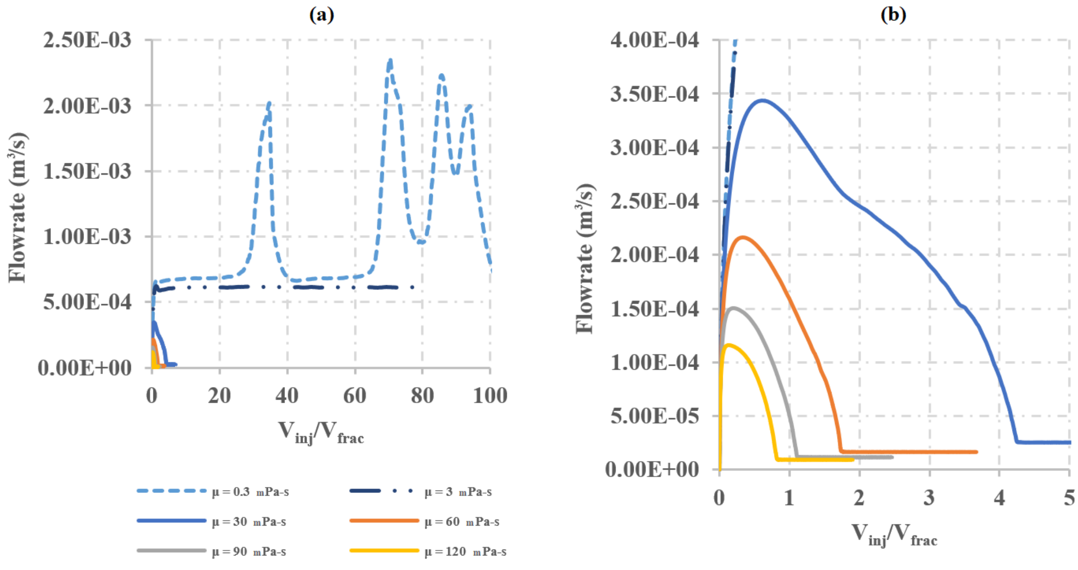

Figure 4: Flowrate at the fracture outlet with various fluid viscosities. (a) Comparison of all six varying cases where it exhibits significant fluid loss on the two least viscous fluids. (b) A closer look at the four most viscous fluids where successful bridging occurs.

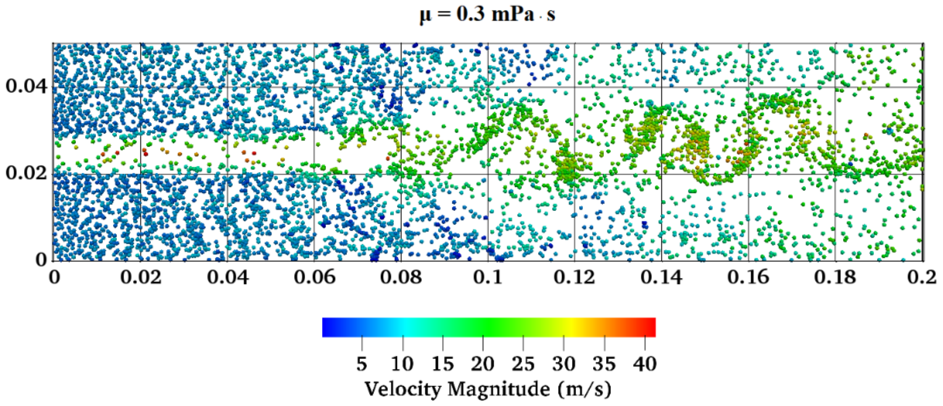

Figure 5: Turbulent flow attributed to ultra-low fluid viscosity with velocity as high as 40+ m/s in a rapid and distorted movement.

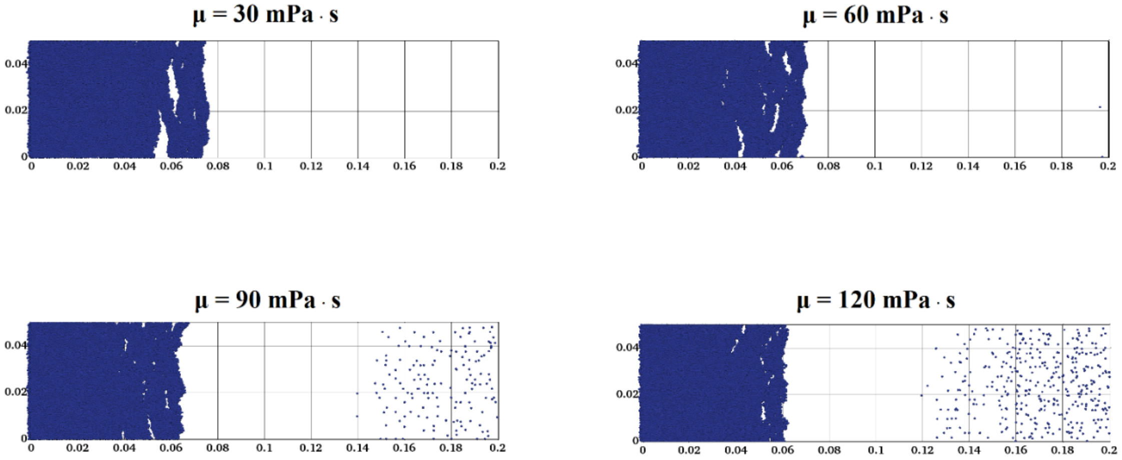

Figure 6: Successful bridging of the four most viscous fluids with similar bridging locations. All snapshots presented at the end of one second where the remaining frontal particles, in higher viscosity cases (90 and 120 mPa·s), move relatively slow.

4.3 Particle Size Degradation due to Temperature Related Issues

As mentioned before, size degradation plays a significant role in effectively sealing a fracture. It is key that cost effective designs must take into consideration the proper particle size and distribution to effectively bridge a fracture. Seven simulation cases of different particle sizes are run. All of them display the initial packing around the same dimensionless volume shown in **Figure 7**. This is most likely due to having the same fluid viscosity. Flowrates peak at around $V_{inj}/V_{frac} = 0.4$ and decrease depending on how fast the complete seal is formed. Although sealing results are obtained for all cases, the sealing mechanisms can be categorized into two types. For diameters equal or less than the fracture outlet, the sealing mechanism is described in section 4.1. For diameters larger than the fracture outlet, bridging occurs simply because the particles are not able to pass through. It is shown in **Figure 8** that the bridging front of each case situates closer to the fracture inlet as particle size increases until its diameter becomes larger than fracture outlet. For larger diameters, 0.6 to 0.9 mm, bridging occurs at the location whose width is equal to particle diameter.

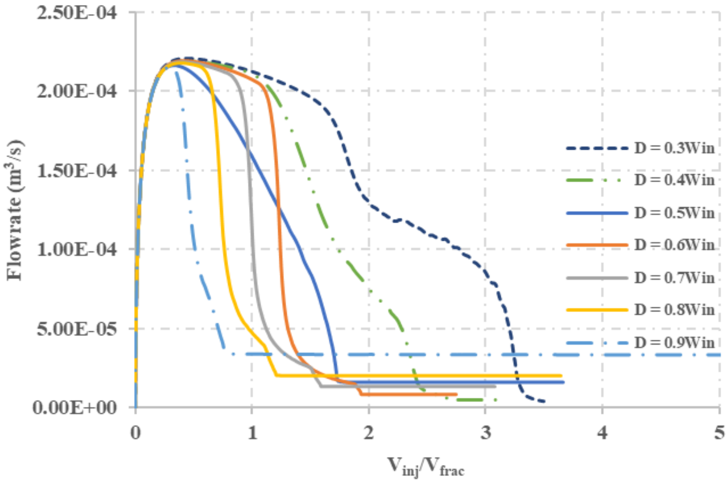

Figure 7: Flowrate at fracture outlet on seven different particle diameters from 0.3 to 0.9 mm particle diameters. Successful bridging in all cases, especially with the two smallest diameter, 0.3 and 0.4 mm. Note that outlet width = 5 mm, one-half of inlet width.

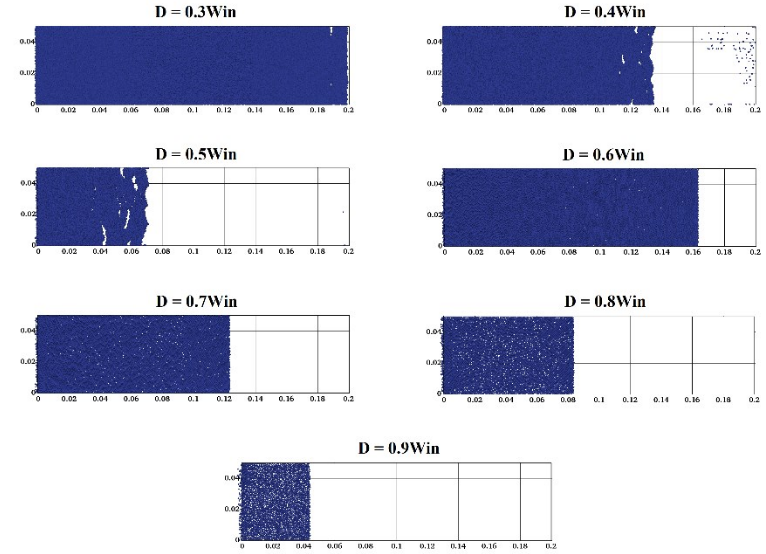

Figure 8: Successful bridging in all simulated particle diameters. For bridging of the three smallest diameter (0.3, 0.4, and 0.5 mm), the bridging front moves closer to the inlet with larger particle size. For sizes from 0.6 to 0.9 mm, bridging happens due to its size being larger than the outlet.

4.4 Thermal Influence on Friction Coefficient

Particle-particle friction and particle-fracture wall friction are factors to be considered at elevated temperatures. Particles are easily flushed to the outlet for low friction coefficient LCMs to bridge a fracture. Bridging occurs in high coefficient cases as shown in **Figure 9**. However, the bridging locations and associated fluid losses are similar for the high coefficient cases. This is possibly because all of their initial buildup of force chains starts in the same location close to the inlet, and thus similar results are obtained.

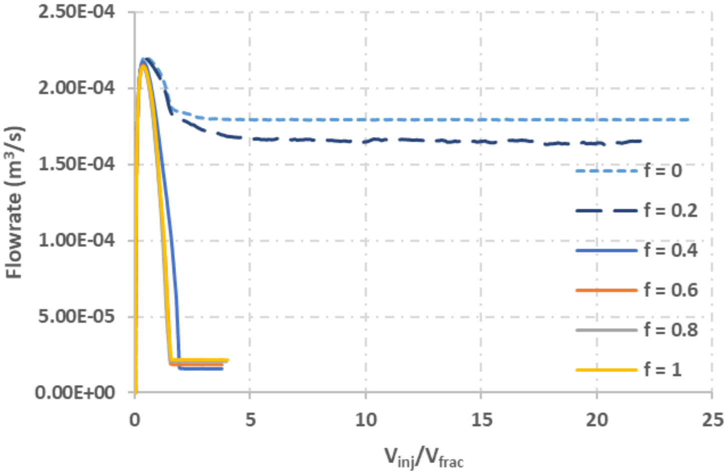

Figure 9: Flowrate at fracture outlet on five different friction coefficients. For coefficient of 0 and 0.2, there is not enough interparticle forces to form a proper seal. For coefficient of 0.6, 0.8, and 1, bridging occurs in almost the same locations for these cases.

4.5 Thermally Induced Reduction of Young's Modulus

Particle elasticity, Young's modulus, can affect fracture sealing capability. Harder particles result in earlier bridging, as shown in **Figures 10** and **11**. Rigid LCMs, with Young's modulus of 10+ GPa, bridges in a very short period and forms a seal close to the fracture inlet. Softer materials have a sealing position that is much different than the rigid ones. Sealing positions are further out towards the fracture outlet. Such differences between the rigid and soft materials come from the fact that LCMs undergo rapid collisions and abrasion. During the transport process in the fracture, soft particles in the confined space experience several bridging events whereas hard particles only need one attempt for bridging.

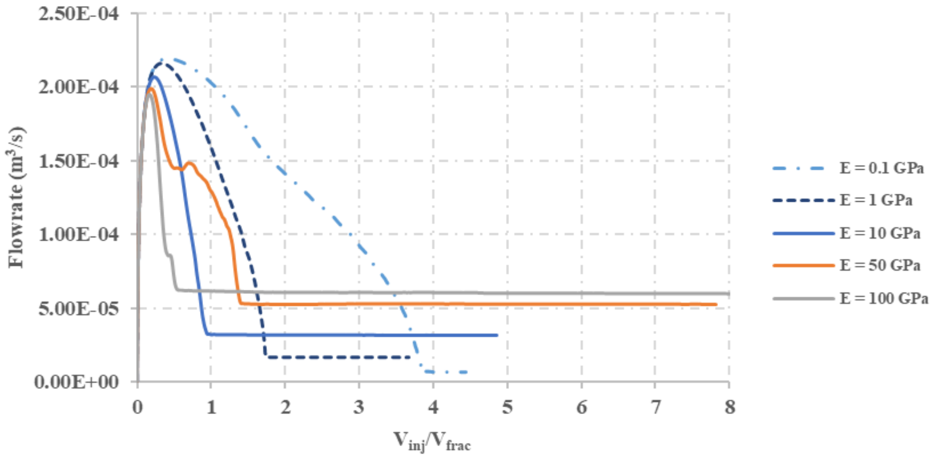

Figure 10: Flowrate at fracture outlet from various Young's modulus. Two softer materials (0.1 and 1 GPa) experience a longer bridging period whereas rigid particles bridge in a very short time.

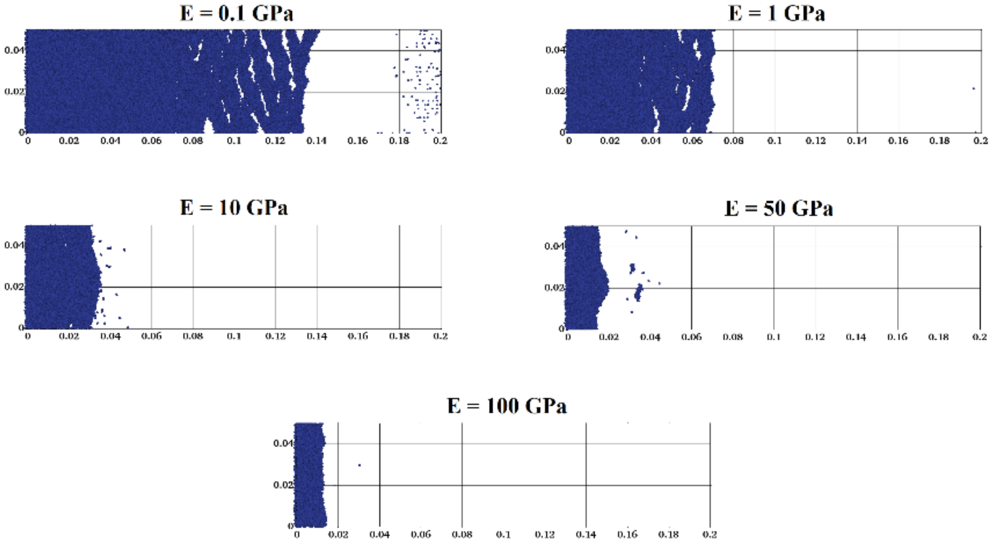

Figure 11: Successful bridging in all simulated cases of Young's modulus. Bridging location is closer to fracture inlet with more rigid LCMs or higher Young's modulus.

5. CONCLUSIONS

Parametric studies have been conducted to study LCM transport in drilling fluids at elevated temperatures. A developed model of CFD-DEM is employed to simulate the fracture sealing phenomenon in a monodispersed particle-fluid system. Thermally induced material degradation includes fluid viscosity and particle mechanical properties. Fluid viscosity, particle mechanical strength, and particle size usually decline at elevated temperatures. It is found that differences in viscosity can greatly affect the fracture sealing capability. The bridging location appears to be only minimally affected by change in viscosity.

Size degradation is also aggravated by elevated temperatures. Smaller particles can bridge in a deeper location. It is found that particle diameter of 0.3 mm (3/5 of the outlet width) exhibits successful bridging from the fracture outlet all the way to the fracture inlet. Lastly, Young's modulus is another important factor that greatly influences sealing mechanisms. Rigid granular particles tend to bridge in a shallower fracture zone whereas softer materials penetrate and bridge in a deeper zone.

ACKNOWLEDGEMENT

This material is based upon work supported by the U.S. Department of Energy's Office of Energy Efficiency and Renewable Energy (EERE) under the Geothermal Program Office, Award Number DE EE0008602. The authors appreciate DOE support.

REFERENCES

Arena, U., D'Amore, M., and Massimilla, L.: Carbon Attrition during the Fluidized Combustion of Coal, *AlChE Journal*, **29**, (1983), 40-49.

Avci, E. and Mert, B. A.: The Rheology and Performance of Geothermal Spring Water-Based Drilling Fluids, *Geofluids*, (2019), 1-8.

Carson, C. C. and Lin, Y. T.: Impact of Common Problems in Geothermal Drilling and Completion, Annual Geothermal Resources Council Meeting, San Diego, California, USA, October 11, (1982).

Cole, P., Young, K., Doke, C. et al.: Geothermal Drilling: A Baseline Study of Nonproductive Time Related to Lost Circulation, *Proceedings*, 42nd Workshop on Geothermal Reservoir Engineering, Stanford University, Stanford, CA (2017).

Cundall, P. A. and Strack, O. D. L.: A Discrete Numerical Model for Granular Assemblies, *Géotechnique*, **29**, (1979), 47-65.

Di Felice, R.: The Voidage Function for Fluid-Particle Interaction Systems, *International Journal of Multiphase Flow*, **20**, (1994), 153-159.

Finger, J. and Blankenship, D.: *Handbook of Best Practices for Geothermal Drilling*, (2010).

Goniva, C., Kloss, C., Deen, N. G. et al.: Influence of Rolling Friction on Single Spout Fluidized Bed Simulation, *Particuology* **10**, (2012), 582-591.

Goodman, M. A.: *Lost Circulation in Geothermal Wells: Survey and Evaluation of Industry Experience*, (1981).

Issa, R. I.: Solution of the Implicitly Discretised Fluid Flow Equations by Operator-Splitting, *Journal of Computational Physics*, **62**, (1986), 40-65.

Kang, Y., Tan, Q., You, L. et al.: Experimental Investigation on Size Degradation of Bridging Material in Drilling Fluids, *Powder Technology*, **342**, (2019), 54-66.

Kloss, C., Goniva, C., Hager, A. et al. 2012. Models, Algorithms, and Validation for Opensource DEM and CFD-DEM, *Progress in Computational Fluid Dynamics* **12**, (2012), 140-152.

Lavrov, A.: *Lost Circulation: Mechanisms and Solutions*, (2016).

Lin, C.-L. and Wey, M.-Y.: Influence of Hydrodynamic parameters on Particle Attrition during Fluidization at High Temperature, *Korean Journal of Chemical Engineering*, **22**, (2005), 154-160.

Loeppke, G. E., Glowka, D. A., and Wright, E. K.: Design and Evaluation of Lost-Circulation Materials for Severe Environments, *Journal of Petroleum Technology*, **42**, (1990), 328-337.

Mansour, A. K., Ezeakacha, C., Dahi Taleghani, A. et al.: Smart Lost Circulation Materials for Productive Zones, SPE Annual Technical Conference and Exhibition, San Antonio, Texas, USA, October 9-11, (2017).

Mansour, A. K. and Dahi Taleghani, A.: Smart Loss Circulation Materials for Drilling Highly Fractured Zones, SPE/IADC Middle East Drilling Technology Conference and Exhibition, Abu Dhabi, UAE, January 29-31, (2018).

Messenger, J. U.: *Lost Circulation*, (1981).

Mohammed, A. S.: Effect of Temperature on the Rheological Properties with Shea Stress Limit of Iron Oxide Nanoparticle Modified Bentonite Drilling Muds, *Egyptian Journal of Petroleum*, **26**, (2017), 791-802.

Peng, Z., Doroodchi, E., Luo, C., and Moghtaderi, B.: Influence of Void Fraction Calculation on Fidelity of CFD-DEM Simulation of Gas-Solid Bubbling Fluidized Beds, *AlChE Journal*, **60**, (2014), 2000-2018.

Wang, F., Tan, X., Wang, R. et al.: High Temperature and High Pressure Rheological Properties of High-Density Water-Based Drilling Fluids for Deep Wells, *Petroleum Science*, **9**, (2012), 354-362.

Zhu, H. P., Zhou, Z. Y., Yang, R. Y., and Yu, A. B.: Discrete Particle Simulation of Particulate Systems: Theoretical Developments, *Chemical Engineering Science*, **62**, (2007), 3378-3396.

Zhu, H. P., Zhou, Z. Y., Yang, R. Y., and Yu, A. B.: Discrete Particle Simulation of Particulate Systems: A Review of Major Applications and Findings, *Chemical Engineering Science*, **63**, (2008), 5728-5770.